Infection-on-Chip: an *in vitro* human vessel to study *Neisseria meningitidis* colonization and vascular damages

Léa Pinon[1], Mélanie Chabaud[2*], Pierre Nivoit[1*], Jérôme Wong-Ng[2*], Tri Tho Nguyen[2], Vanessa Paul[1], Sylvie Goussard[1], Emmanuel Frachon[2], Dorian Obino[1], Samy Gobaa[2], Guillaume Duménil[1]

[1]Institut Pasteur, Université Paris Cité, INSERM UMR1225, Pathogenesis of vascular infections, F-75015 Paris, France.

[2]Institut Pasteur, Université Paris Cité, Biomaterials and Microfluidics platform, F-75015 Paris, France.

*Equal contribution

Abstract

Bloodstream infections leading to sepsis are a life-threatening condition and remain difficult to treat, however, *in vitro* experimental models that reflect their key features are still lacking. We here developed a photoablation-based 3-dimensional, microfluidic model of meningococcal vascular colonization, which allows to study cardinal features of the bacteria-blood vessel interaction within controllable vascular geometries. Meningococci are Gram-negative human-specific bacteria responsible for meningitis and a severe form of sepsis that is associated with vascular damages, referred to as *purpura fulminans*. The infection-on-chip device is used to quantitatively assess bacterial adhesion and proliferation at high spatio-temporal resolution in a physiologically relevant microenvironment. In addition, we here show that vascular colonization by meningococci in our Infection-on-Chip device recapitulates key features of disease progression, including vascular leakage and the recruitment of neutrophils to sites of infections, mirroring results obtained using our previously described human skin xenograft mouse model. As a result, our Infection-on-chip platform provides a robust alternative approach to the use of animal and 2D cellular models, opening the path to the better understanding of

disease progression and testing innovative therapeutics in an *in vitro* but physiologically relevant environment.

Introduction

While antibiotics constitute a highly efficient treatment against most bacterial infections, antimicrobial resistance is on the rise and represents a major global public health threat [1]. The development of novel therapeutic strategies requires a better understanding of the mechanisms underlying infectious diseases and the development of robust experimental models that recapitulate the hallmark features of infection to test potential treatments. In this study, we describe an *in vitro* photoablation-based 3-dimensional, microfluidic model for the pathological interaction of meningococci with human blood vessels, a central step of sepsis and meningitis caused by this Gram-negative bacterium.

Invasive meningococcal disease falls into the broad category of systemic diseases. Such infections result from the access of bacteria to the bloodstream, a situation referred to as bacteremia. While circulating through blood vessels, pathogenic bacteria can trigger sepsis, a life-threatening inflammatory syndrome [2]. Systemic infections, including sepsis, remain difficult to treat and the lack of physiologically relevant *in vitro* experimental models reproducing the key features of these infections to better understand pathogenesis and propose new treatments. Sepsis is typically caused by *Staphylococcus aureus, Streptococcus pyogenes, Klebsiella spp., Escherichia coli, Pseudomonas aeruginosa* and our model system, *Neisseria meningitidis.* All lead to different types of sepsis (e.g. fulminant, acute, subacute, chronic) depending on their biological properties and virulence factors [2]. *N. meningitidis* is responsible for meningitis but also for an acute form of sepsis, referred to as *purpura fulminans,* typically associated with purpuric marks on the skin, underlying perturbations in vascular function [3, 4].

Clinical studies have provided key elements of *N. meningitidis* pathogenesis leading to *purpura fulminans* that need to be reproduced in a relevant infection model. Histological studies of postmortem samples have shown that bacteria are found primarily inside blood vessels of different organs, including

51 the liver, the brain, kidneys, and the skin. Bacteria are typically found either associated with the
52 endothelium on the luminal side in tight aggregates or inside neutrophils [5]. The infection is associated
53 with signs of vascular function perturbations, including congestion, intravascular coagulation, and loss
54 of vascular integrity [6]. The presence of bacteria within the lumen of blood vessels is also associated
55 with an inflammatory infiltrate composed of neutrophils and monocytes [7]. A valid model of
56 meningococcal infection should thus reproduce the interaction of bacteria with the endothelium and
57 immune cells, as well as infection-induced vascular damage.

58 Meningococcal infections are highly species specific to humans, thus a human skin xenograft mouse
59 model of meningococcal intravascular infection was necessary to reproduce key feature of
60 meningococcal infection [8, 9, 10]. This model was instrumental in demonstrating the importance of
61 bacterial type IV pili for vascular colonization and was used for testing novel treatment strategies [8,
62 11]. While providing the proper tissue context for meningococcal infection, this model is dependent on
63 access to fresh human skin, complex surgical procedures, and animal use.

64 Another popular experimental approach involves the use of endothelial cells in culture where interaction
65 between *N. meningitidis* and single human cells are studied on flat 2D surfaces [12-14]. Such models
66 have been used to decipher the molecular interplay underlying bacteria-bacteria and bacteria-
67 endothelial cells interactions and have been essential in characterizing the host cell reorganization upon
68 bacterial adhesion [13, 14]. This notably includes the remodeling of the plasma membrane with the
69 formation of filopodia-shaped protrusions that stabilize the microcolony in the presence of flow-induced
70 shear stress [15]. The actin cytoskeleton has been also shown to be highly reorganized underneath
71 bacterial microcolonies, forming a structure reminiscent of a honeycomb, also called cortical plaque
72 [16]. Although easy-to-use, 2D models do not recapitulate the geometry of the vascular system, nor the
73 proper molecular signaling of inflammation found in a 3D micro-environment [17]. An *in vitro* model
74 recapitulating key features of meningococcal infection in a biologically relevant environment is
75 therefore still lacking.

76 Producing a synthetic yet functional human vasculature has been investigated heavily in the last decade
77 including by establishing a 3D vascular system inside a hydrogel loaded onto a microfluidic chip [18,
78 19, 20]. Endothelial cells are embedded into hydrogels to self-assemble into interconnected tubes.
79 Although delivering functional vasculature, this method does not allow the control over the produced
80 vascular geometry. Other methods consist in loading cells into pre-formed structures using molding
81 [21, 22] or viscous fingering [23]. These approaches allow the formation of large patterns (120-150 µm)
82 and straight structures, but vessels in tissues are tortuous, ramified and can be as narrow as 10 µm in
83 diameter. Finally, photoablation techniques were also used to produce synthetic vasculature [24, 25,
84 26]. This technique comes with several advantages including maximal control over the produced
85 geometry and the capacity to mirror *in vivo* structures.

86 In this study we have used a home-made laser ablation setup to engineer a vascular system on-chip with
87 tunable parameters to generate vessels of various shapes and sizes, hence reflecting the complexity of
88 the *in vivo* vascular system. Conditions were optimized to reproduce cardinal features of meningococcal
89 infections, bacterial adhesion, cellular remodeling, vascular damage and interaction with neutrophils.
90 The human skin xenograft-based animal model was used as a gold standard all along the study to
91 establish the infection-on-chip model. The proposed approach offers a powerful alternative to animal
92 models in the field of host-pathogen interaction and consists of a relevant tool for quantitative studies
93 in a realistic environment.

94

95 **Results**

96 **Replicating the *in vivo* vascular geometry using photoablation**

97 To study the ability of *N. meningitidis* to colonize vessels and induce subsequent vascular damage in
98 relevant vascular geometries, we developed a Vessel-on-Chip (VoC) based on the photoablation
99 technique. The chip displays a center channel (hydrogel) connected with two larger lateral channels
100 (culture media, cells). The whole structure is made of poly-dimethyl siloxane supported by a glass

101 substrate. The center channel is filled with collagen I as previously used to mimic extracellular matrix
102 in *in vitro* models [23]. The photoablation process consisted of carving the collagen I matrix at the
103 center of the microfluidic chip with a focused UV-LASER beam (Fig. 1A and 1B). Endothelial cells
104 introduced in the collagen-carved scaffold formed a vascular lumen (Fig. 1B). The lateral channels
105 remain open to ensure regular liquid flows for nutrient replenishment and the further introduction of
106 bacteria and immune cells. Throughout this study, our developed *in vitro* model was compared to the
107 *in vivo* situation in mouse ear vessels and in human vessels of human skin xenografted mice (Fig. 1C).

108 *In vivo*, extracellular matrix is crucial because provides structural and organizational stability of
109 vascular tissue [27]. It acts as a chemical substrate to ensure cell adhesion, and mechanical support
110 which can be remodeled in the case of angiogenesis [28]. In our VoC, the vessel scaffolding is ensured
111 by collagen I, the most abundant protein found in extracellular matrix [29]. First, we investigated the
112 impact of ECM concentration on vascular morphology. After 48h of culture in the VoC, cells spread
113 over the tube edges, deformed the squared carved scaffold in cross-section and finally shaped round
114 vascular lumens (Fig. S1A). However, we also observed sprouting across collagen matrix along the
115 vessel. In a 2.4 mg/ml collagen matrix (FujiFilm, see *Material and Method* section), endothelial cells
116 formed multiple sprouts along the vessel length (Fig. 1D). For the same initial vessel dimensions (Fig.
117 S1B and S1C), the formation of sprouts decreased with increasing collagen concentration. Sprouting
118 was abolished at 4 mg/ml and beyond (Corning, see *Material and Method* section) (Fig. 1D and and
119 1E). To understand the origin of such ability to sprout, we measured visco-elasticity properties of the
120 hydrogels at different concentrations (Fig. S1D). The most concentrated collagen solutions (4 and 6
121 mg/ml) displayed the highest Young's moduli (75 and 250 Pa), which correlate with a decrease of
122 vascular sprouting. The 3.5 mg/ml from the Corning solution displayed the same stiffness as the 2.4
123 mg/ml from FujiFilm solution (50 Pa), while they had different effects on the number of sprouts.
124 Altogether, these results suggest endothelial cell sprouting is determined by both the concentration and
125 the composition of collagen – that, we assume, may vary cross-linkage and pore size.

126 Once collagen matrix was optimized, we obtained endothelial-embedded circular tubes although
127 photoablation carving generates square sections (Fig. 1F). The photoablation approach allows to
128 generate any 3D geometry. We were thus able to form more complex structures derived from intravital
129 imaging (Fig. 1G). For instance, a vascular branching point observed and measured *in vivo* in a mouse
130 could be reconstituted in the VoC. The photoablation technique combined with appropriate extracellular
131 matrix properties thus allows the assembly of *in vivo*-like structures.

132

133 **The Vessel-on-Chip devices provide permeability levels similar to those observed *in vivo***

134 A key feature of meningococcal infection is its association with a loss of vascular permeability.
135 Relevant infection models should therefore allow the observation and quantification of this vascular
136 integrity loss. While previously described Vessel-on-Chip technological solutions aim at mimicking
137 physiological permeability [27], comparison with *in vivo* values is rarely indicated. Here, we evaluated
138 the vascular permeability in both VoC and animal models. Since the integrity and permeability is
139 dependent on cellular junctions, we first visualized these structures in the chips. After 48h, cells formed
140 thin and uniform junctions as seen with PECAM-1 straining (Fig. 2A), confirming the cohesiveness of
141 the tissue-engineered vessel. We also found that endothelial cells also secrete collagen IV (Fig. 2B)
142 which is the main component of the basement membrane, providing cell and tissue support and acts as
143 a platform for complex signaling [30].

144 To evaluate vascular integrity functionally, we conducted imaging-based permeability assays using
145 fluorescent 150 kDa dextran (Fig. 2C) by comparing intensity of fluorescence inside and outside VoC.
146 We observed that vessels forming sprouts tended to display a high permeability while the absence of
147 sprouting correlated with low permeability. Permeability decreased by about 10-fold between
148 conditions using 2.4 and 4 mg/ml of collagen. At high concentration of collagen, values of permeability
149 were close to those measured in the mouse ear (Fig. 2D). With concentrations of 4 mg/ml of collagen
150 no evidence of leakage could be seen for periods as long as 10 minutes, as observed *in vivo*. Altogether,

151 these results show that our VoC supported by a highly concentrated collagen matrix forms a stable
152 physical barrier with a low permeability close to the *in vivo* conditions.

153

154 **_N. meningitidis_ colonize the vascular microenvironment in the Vessel-on-Chips**

155 Availability of *in vitro* tight vessels of controlled geometries allowed us to observe meningococcal
156 infection in a 3D environment mimicking *in vivo* conditions. Bacteria were introduced into the
157 microfluidic device and could circulate through the lumen of VoC (Fig 3A). After a period of 3 hours,
158 we found that meningococci could attach to the vascular wall (Fig. 3B) as observed in infected patients
159 and in the previously described skin xenograft model [13]. Bacteria formed 3D microcolonies of
160 different sizes ranging from a few to tens of microns. They covered the endothelium and followed the
161 curved shape of the vessel along the section and length of the VoC. Adhesion occurred both in straight
162 and *in vivo*-like structures, as observed in the original geometry *in vivo* although with higher resolution
163 allowing visualization of single bacteria (Fig. 3C). Overall, the infection-on-chip model recapitulates
164 meningococcal vascular colonization in 3D and enables high–resolution fluorescence microscopy to
165 monitor infection.

166

167 **Endothelial cell in the Vessel-on-Chips respond to flow-mediated shear stress**

168 Flow-mediated shear stress is a key factor that shapes endothelial cells physiology [31] as well as *N.*
169 *meningitidis* adhesion along the endothelium [32]. To define the wall shear stress that needs to be
170 applied in our system, we performed particle image velocimetry (PIV) in live mice, by injected
171 fluorescent beads in the blood circulation (Fig. S2A). Figure S2B shows that the flow rate increases
172 with vessel diameter, consistently with [33]. We found that the endothelial cells are submitted to an
173 average wall shear stress of 1.57 Pa in arterioles while they sense a value of 0.31 Pa in venules (Fig.
174 4A) consistently with previous measurements [34, 35, 36].

175 We then assessed in the VoC, how endothelial cells respond to a venule-like flow (Fig. 4B). The impact
176 of the resulting flow on endothelial cell physiology was determined by assessing the orientation and
177 alignment of cell nucleus, known to be a sensor of blood flow direction [36]. There, we found that under
178 physiological flow conditions, nuclei tended to elongate and align along the direction of the flow (Fig.
179 4C and S2C). Circular plots show a progressive narrowing distribution upon flow exposure (0h to 24h
180 of flow). To compare the statistical dispersion in different conditions, interquartile range (IQR) related
181 to orientation distribution was assessed for each vessel (Fig. 4D). We showed that nuclei oriented along
182 the flow in 24h, to reach an average orientation value of 15º close to *in vivo* conditions (Fig. 4D and
183 S2D). Likewise, nucleus elongation, assessed by the length/width ratio, reached the *in vivo* average
184 value of 2 after 24h of flow (Fig. 4E and S2E). This suggests a homogenization of nuclei orientation
185 and elongation for a longer flow exposure. Interestingly, vessel diameter decreased when endothelial
186 cells were submitted to flow, while cell density is similar in all conditions (Fig. S2F and S2G). The
187 flow-mediated cell alignment thus tends to prevent VoC deformation without affecting cell density.
188 Altogether, these results show that cells in VoC physiologically respond to mechanical shear stress
189 including by elongating and aligning their nuclei along the flow direction.

190

191 **Liquid flow impacts microbial colony morphology**

192 Before investigating the morphology of *N. meningitidis* infection under flow conditions, we explored
193 the role of type IV pili-mediated adhesion within VoCs by comparing a wild type strain (WT) and a
194 mutant deprived of pili deficient in the *pilD* gene. We observed that after 3h of infection under flow
195 conditions (Fig. 5A), VoC deviced infected with *pilD* contained a few small *N. meningitidis* aggregates
196 while infection the with WT strain led to the formation of numerous and large colonies (Fig. 5B, S3A
197 and S3B) on the vascular walls. This shows that as observed in the human skin xenograft model, and
198 2D cell culture models, type IV pili are also essential for adhesion in the VoC.

199 We observed that flow induces a shape change of the microcolonies in the VoC (Fig. 5C and 5D).
200 Bacterial colonies are more elongated and oriented along the vessel length (flow direction), as observed
201 in *in vivo* conditions (Fig. 5C and 5D). This shear stress-driven morphology change is likely due to the
202 viscous behavior of bacterial aggregates [14].

203 Colony expansion was then assessed under flow by monitoring the increase of surface area covered by
204 adherent bacteria over time (Fig. 5E). Individual colonies, represented by the thin shaded curves (Fig.
205 5E), in both environments (VoC and mouse model) followed a mean linear tendency (solid curve) which
206 likely represents a combination of proliferation, detachment and further adhesion of circulating bacteria.
207 We showed that microcolony expansion time in both VoCs and human skin-grafted mice are similar
208 (Fig. 5F). Interestingly, the time for colony surface doubling is about 20 min in those models, while in
209 agar pad, the division time of *N. meningitidis* is about 30-40 min [38]. Further work will be needed to
210 distinguish between an increased catching of circulating bacteria or that bacteria divide faster in these
211 conditions [14]. Fusion of colonies, as shown in figures S3C and S3D and referenced in [39] is another
212 factor in the process. Nevertheless, the introduction of flow is thus not only important to recapitulate
213 endothelial cell physiology but also to faithfully reproduce conditions experienced by bacteria during
214 infection leading to rapidly growing elongated colonies.

215

216 **Flow-induced aligned actin stress fibers are reorganized below bacterial microcolonies**

217 *N. meningitidis* bacterial colonies have been described to reorganize plasma membrane and actin
218 cytoskeleton in 2D models [40, 41, 42]. We next investigated whether this was the case in the 3D
219 environment, under flow conditions. Endothelial cells in the perfused VoC are submitted to flow-
220 induced mechanical stress which is known to affect the state and behavior of the actin cytoskeleton [43,
221 44], and this could shape bacteria-induced responses. First, we confirmed that, while in absence of flow
222 actin stress fibers displays random orientations, in the presence of flow stress fibers were highly
223 organized and aligned (Fig. 6A and 6B). Strikingly, we observed that actin fiber orientation occurs as

224 rapidly as 2h post-introduction of flow. The rapid adaptation of actin fibers due to mechanical stress is
225 confirmed by the strong decreases in IQR when shear stress increases (Fig. S4A), indifferently of the
226 time (2h or 24h).

227 Despite the flow-mediated alignment of F-actin network, we observed that bacterial microcolony
228 induced honeycomb-shaped actin reorganization on endothelial cells lining the VoC (Fig. 6C and 6D).
229 We show that this particular F-actin reorganization is formed under flow conditions and takes the same
230 elongated shape as flow-driven bacterial colonies. After 3h of infection, in these conditions, 65% of
231 colonies already formed the honeycomb-shaped structure while 35% were not forming them (Fig. 6E).
232 F-actin fluorescence intensity under microcolonies were 2-fold higher compared to non-infected area
233 (Fig. 6F) reaching previously observed values in 2D models [45]. The highly organized actin fibers
234 present in the VoC are strongly reorganized by microcolonies, a process that can be quantified by the
235 value of coherency which is indeed decreased by infection (Fig. 6G). The loss of coherency is correlated
236 with the increase of F-actin fluorescence intensity (Fig. S4B). Altogether, these results show that *N.*
237 *meningitidis* actively reorganizes endothelial cell cytoskeleton in VoC under flow conditions despite
238 the presence of a highly organized and aligned F-actin network.

239

240 **The Infection-on-chip device recapitulate the human neutrophil response to *N. meningitidis***
241 **infection**

242 The presence of an inflammatory infiltrate mostly composed of neutrophils in the vicinity of infected
243 vessels is another cardinal feature of meningococcal infection. Previous *in vivo* studies of *N.*
244 *meningitidis* infections have shown the recruitment of neutrophils along infected venules following E-
245 selectin upregulation [11]. We have thus examined the ability of the vessel surrogate to upregulate E-
246 selectin expression upon inflammatory stimuli. While endothelial cells did not express E-selectin at
247 basal conditions (Fig. 7A and 7B), both TNFα stimulation (Fig. 7A) and *N. meningitidis* infection (Fig.
248 7B) led to a massive upregulation of E-selectin expression. Interestingly, infection with the non-piliated

249 *pilD* strain induced a slight E-selectin expression, but less than WT strain showing the importance of
250 adhesion in this process (Fig. S5A and S5B). The expression of E-selectin on *N. meningitidis*-infected
251 endothelium is more spatially heterogeneous than the TNFα-inflamed tissue (Fig. S5C), suggesting a
252 spatial cell to cell heterogeneity in endothelial cells response upon *N. meningitidis* infection that
253 correlates with *in vivo* observations [11].

254 Having shown the upregulation of E-selectin upon TNFα and *N. meningitidis* infection in our VoC
255 model, we next assessed the local recruitment of neutrophils. To this end, we purified human neutrophils
256 from healthy donors' blood, and perfused them under flow conditions (0.7-1 µL/min) in the microfluidic
257 chip (Fig. 7C). The increase in CD62E expression upon *N. meningitidis* infection and TNFα treatment
258 led to neutrophil adhesion (Fig 7D). Quantification of neutrophil numbers per surface area revealed
259 similar number of adhering neutrophils independently of the inflammatory stimulus used, either TNFα
260 or *N. meningitidis* intravascular colonization (Fig. 7D). Similar to our humanized mouse model [8, 11,
261 45], we observed that TNFα treatment induced neutrophil adhesion cascade, with major steps consist
262 of rolling, arrest, and crawling of human neutrophils on the endothelium (Fig. S5D and S5E) [46].
263 Remarkably, we noted the bacteria-induced phagocytic events, comparable to those observed *in vivo*
264 (Fig. 7F). Altogether, these results show that the developed VoC provides a suitable micro-environment
265 to recapitulate the neutrophil recruitment and innate immune response upon inflammation and *N.*
266 *meningitidis* infection.

267

268 **Discussion**

269 To overcome the lack of suitable *in vitro* models of vascular infection, we have developed an *in vitro*
270 3D human Vessel-on-Chip microfluidic-based model that recapitulates the vascular environment
271 encountered by *N. meningitidis* during intravascular colonization. This model recapitulates the key
272 features of meningococcal infection, as assessed by comparing it with the *in vivo* human skin xenograft
273 mouse model. Thanks to photoablation, we controlled the size and shape of the UV-carved hydrogel

274 scaffolds, thus we could replicate tissue-engineered in VoC of *in vivo* structures that have been extracted
275 from intravital images. While photoablation is usually considered to be too slow to be practical [20],
276 the photoablation process we have developed is fast, and the replication of the more complex presented
277 geometry has been achieved in about 1 minute allowing rapid preparation of multiple devices. The
278 system presents a low permeability and is easily perfusable, allowing to reproduce shear stress levels
279 found in venules or arteries *in vivo*. The presence of shear stress leads to visible cellular reorganization
280 which align parallel to the flow as observed *in vivo*. The actin cytoskeleton rapidly reorganizes to form
281 stress fibers parallel to the flow as early as 2h post-introduction of flow. Nuclei change shape and align
282 along the flow only 24h after flow introduction, possibly as a consequence of the actin reorganization
283 [47]. Junctions between cells are also clearly visible. These results emphasize that the approach selected
284 provides vessels with endothelial cells in the physiological conditions found *in vivo* providing a realistic
285 micro-environment to further reconstitute *N. meningitidis* vascular infection.

286 *N. meningitidis* introduced in the VoC readily adheres along the endothelium and form three-
287 dimensional colonies which increase in size with the same speed as found *in vivo*. By comparing wild
288 type piliated and non-piliated strains (*pilD*), we showed that type IV pili are necessary for adhesion and
289 microcolony formation in VoC under flow conditions, consistent with the *in vivo* studies [48, 49]. Type
290 IV pili not only mediates steps from early adhesion to aggregation in microcolonies [39], but also
291 control the visco-elastic properties and shape of bacterial aggregates [50, 51]. Consistently, we found
292 that in the 3D *in vitro* vessels and under flow, bacterial aggregates tend to take elongated shapes rather
293 than the circular shapes found in 2D models. This change of shape is likely due to the impact of shear
294 stress on these visco-elastic structures and might potentially affect the dynamics of vascular
295 colonization by adherent meningococci. Combined with the dynamic visco-elastic property of the *N.*
296 *meningitidis* aggregates [14], which helps bacteria adapt to their environment, we assume that flow is
297 helpful for bacterial infection propagation as it spreads out colonies on the endothelium.

298 Meningococcal colonization of the VoC also recapitulates the drastic reorganization of the actin
299 cytoskeleton, adopting the characteristic form of the honeycomb-shaped cortical plaque [15]. Although

300 such structures have been described in 2D models, it is particularly striking in this context since the
301 actin cytoskeleton completely reorganized the present of flow in this geometry. *N. meningitidis* is thus
302 able to completely reorient the actin cytoskeleton despite the presence of flow and a highly organized
303 and parallel actin network. The observed impact of type-IV pili on the host cell in our VoC underlines
304 its importance for colony stabilization against flow-mediated wall shear stress in the bloodstream [39,
305 52].

306 The laser ablation approach used here will allow future studies to explore the impact of vessel
307 morphology on bacterial adhesion. Indeed, vascular geometry might disturb streamlines and participates
308 in bacterial colonization in strategic low velocity regions [31]. Our system, highly tunable allows the
309 design of vessel surrogate of various sizes and shapes, thus representing a unique tool to further explore
310 how vascular geometry and shear stress impacts T4P-mediated vascular colonization in healthy [53, 54]
311 and pathological (e.g., diabetes [55, 56]) conditions, by testing bacterial adhesion in vessels of different
312 shapes (straight, branched, tortuous).

313 Because of bacterial adhesion, infected vessels lose their integrity and leakage is observed leading to
314 the formation of purpuric marks in the infected patients. Colonization of *N. meningitidis* induces
315 vascular damages beginning with the destabilization of cell-cell junction and cell-extracellular matrix
316 interaction [39] inducing a leakage. We have shown that VoC maintain their integrity in healthy
317 conditions with low permeabilities similar to those found in the mouse. *In vivo*, such infection induced
318 vascular alterations is linked to the triggering of intravascular coagulation [38, 57]. Coagulation has
319 been recently recapitulated in 3D vascular models in healthy conditions [58] and could be extended in
320 our system in future studies.

321 Finally, we have explored the human neutrophil response in contact with infected human endothelium
322 in VoC. We first showed that infection leads to E-selectin surface upregulation in our *in vitro* system,
323 as previously demonstrated in the human skin xenograft mouse model [13]. Human neutrophils
324 introduced in the lumen of the VoC adhere to the infected endothelium, roll and then crawl as found *in*
325 *vivo*. Furthermore, neutrophils move towards bacteria and actively phagocyte adherent *N. meningitidis*

326 as shown *in vivo.* It should be pointed out that in this case, human neutrophils are interacting with human
327 endothelial cells. This is in contrast with the humanized xenograft model for which mouse neutrophils
328 interact with human endothelial cells [13]. Thus, we offer a valid alternative model to animal
329 experimentation to study the human immune response to intravascular infection.

330 To conclude, our model leveraging engineered microenvironments has a strong potential as an
331 alternative approach that will help us better understand bacterial physio-pathology in realistic infection
332 contexts and to test potential innovative treatments. We have demonstrated that our model is an ideal
333 microenvironment to recapitulate *N. meningitidis* vascular adhesion and microcolony formation in
334 complex vascular morphologies and subsequent pathological consequences. Although the system was
335 optimized for meningococcal infection, this approach paves the way for the study of other pathogens
336 responsible for systemic infections. Vasculature is the main road for systemic infection [59, 60] and
337 bacterial transport toward multiple body environments [61, 62]. We provide the community with an
338 engineering system that could be modulable for a wide range of organisms (e.g., other bacteria, viruses,
339 fungi) and vascular systems (e.g., angiogenesis, capillary beds, arteries), and suitable for quantitative
340 and applied approaches in the field of biophysics and biomedical research (e.g., drug screening). Our
341 model will allow the discovery of overlooked aspects of infections and help the development of novel
342 therapeutic strategies.

343 **Figures**

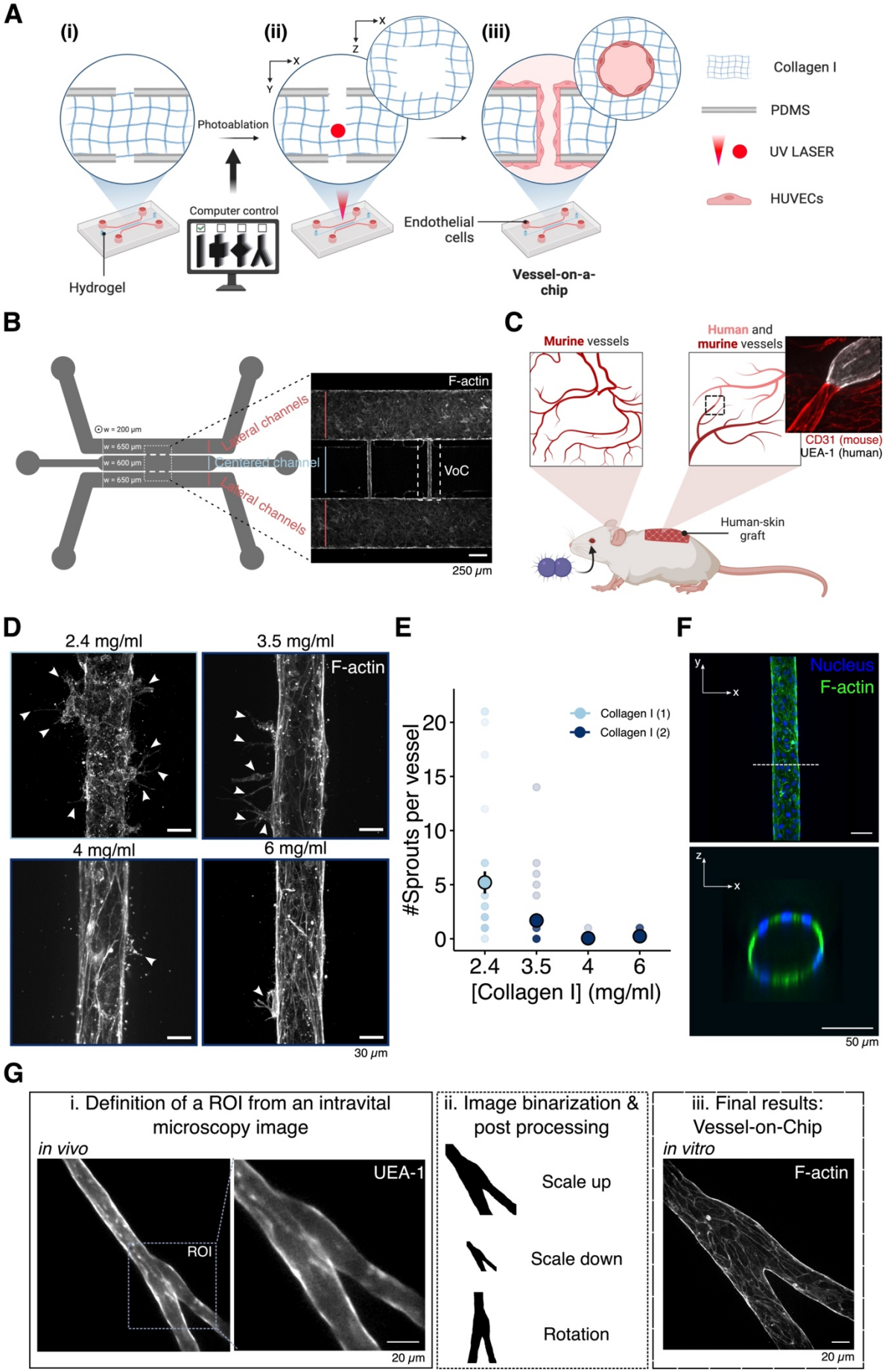
A
(i)
(ii)
(iii)
Photoablation
Computer control
Hydrogel
Endothelial cells
Vessel-on-a-chip
Collagen I
PDMS
UV LASER
HUVECs
B
w = 200 µm
w = 650 µm
w = 600 µm
w = 650 µm
Lateral channels
Centered channel
Lateral channels
F-actin
VoC
250 µm
C
Murine vessels
Human and murine vessels
CD31 (mouse)
UEA-1 (human)
Human-skin graft
D
2.4 mg/ml
3.5 mg/ml
4 mg/ml
6 mg/ml
F-actin
30 µm
E
#Sprouts per vessel
Collagen I (1)
Collagen I (2)
[Collagen I] (mg/ml)
F
Nucleus
F-actin
50 µm
G
i. Definition of a ROI from an intravital microscopy image
in vivo
ROI
UEA-1
20 µm
ii. Image binarization & post processing
Scale up
Scale down
Rotation
iii. Final results: Vessel-on-Chip
in vitro
F-actin
20 µm

Fig. 1: Mimicking the *in vivo* vascular geometry using photoablation

(A) Schematic representation of the development of the VoC: (i) a collagen-based hydrogel is inserted at the center channel of the microfluidic device, (ii) the focused UV-LASER locally carves the chosen geometry within the collagen I matrix, (iii) HUVEC attach on the collagen-carved scaffold. (B) Schematic representation of the microfluidic device and zoom in of the carved region after endothelialization (F-actin). (C) Schematic representation of the animal models assessed in this study: the mouse ear and the human skin-grafted mice. (D) Confocal image of vessel formation on 2.4 mg/ml - 3.5 mg/ml - 4 mg/ml and 6 mg/ml collagen I. The Corning collagen I has been used making the solution from 3.5 mg/ml to 6 mg/ml, and the Fujifilm collagen I has been used to make the 2.4 mg/ml. Each image is representative of one of the highest values of sprouting per condition. (E) Graph representing the number of sprouts per vessel for four collagen I concentrations: 2.4 mg/ml (FujiFilm), 3.5 mg/ml, 4 mg/ml and 6 mg/ml (Corning). Each dot represents one vessel. For each condition, the mean ± s.d. are represented (2.4 mg/ml: 5.20 ± 6.0 - 3.5 mg/ml: 1.69 ± 3.04 – 4 mg/ml: 0.045 ± 0.22 – 6 mg/ml: 0.23 ± 0.43). (F) Confocal images of F-actin and related Z-slice of the tissue-engineering VoC. (G) The photoablation technique to create *in vivo*-like structures: (i) definition of the region of interest to replicate from intravital microscopy images, (ii) image binarization, image post-processing and hydrogel-carving process, (iii) final results: immunostaining of the microfluidic chip.

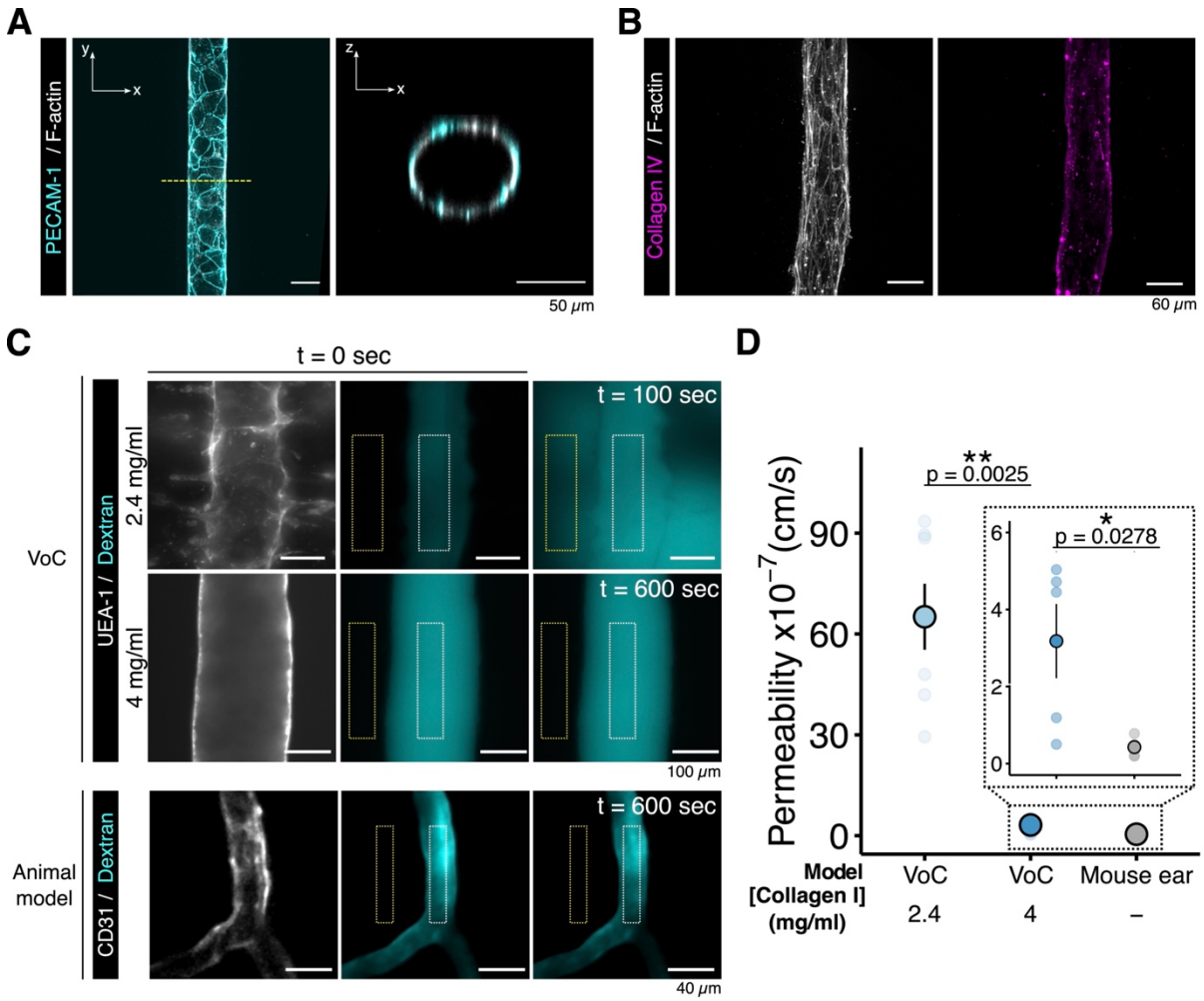

Fig. 2: Vessel-on-Chip devices provide permeability levels similar to those observed *in vivo*

(A) Confocal images of the PECAM-1 junctions and related Z-slice of the tissue-engineering VoC. (B) Confocal images of the collagen IV secretion in the tissue-engineering VoC. (C) Representative confocal images of fluorescent 150 kDa-Dextran (FITC) in the VoC (top) and in the mice ear model (bottom). Yellow and white dashed boxes represent the outside and inside regions of the vascular lumen, respectively, where fluorescence intensity has been measured to determine permeability. (D) Graph representing permeability of 150 kDa-Dextran in the VoC and in ear mice vessels. Each dot represents one vessel. For each condition, the mean ± s.d. are represented (VoC, 2.4 mg/ml: 65.12 ± 26.00 cm/s – VoC, 4 mg/ml: 3.18 ± 2.15 cm/s - *in vivo*: 0.43 ± 0.24 cm/s). All statistics have been computed with Wilcoxon tests.

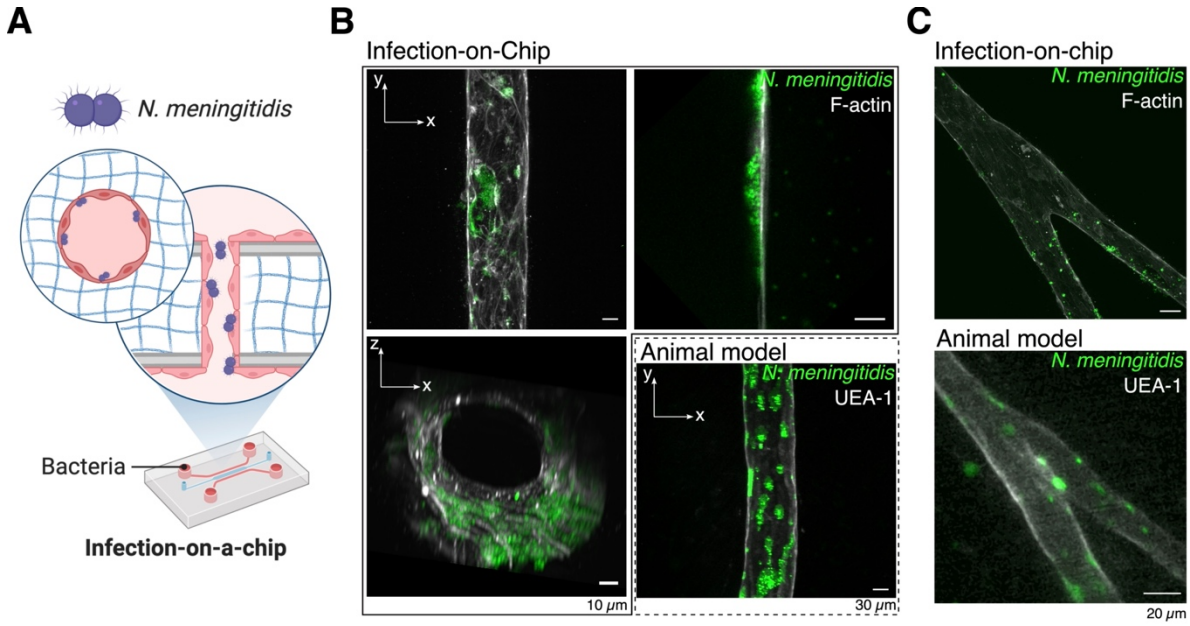

Fig. 3: The Vessel-on-Chip devices are relevant microenvironments for *N. meningitidis* infection

(A) Schematics of the Infection-on-Chip device. (B) Confocal images of infected vessels in the Infection-on-Chip device and in the human skin-grafted mice model. (C) Z-projection intensity of confocal imaging of a branched Infection-on-Chip design and the compared infected human skin-grafted mice vessel.

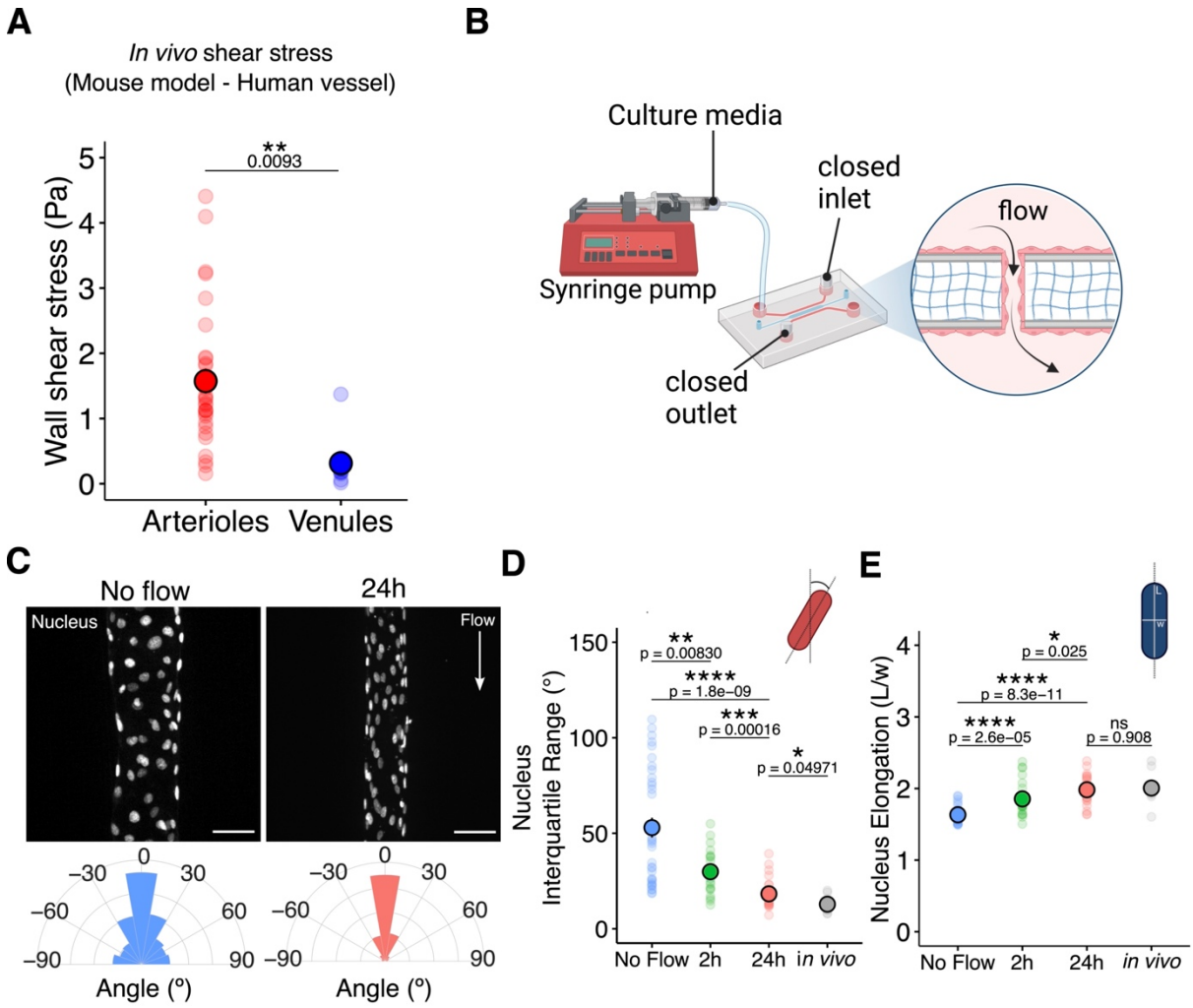

Fig. 4: Introduction of flow inside the Vessel-on-Chip is necessary to reproduce cellular morphological features

(A) *In vivo* wall shear stress measured in arterioles and venules. Each dot represent a vessel. For each condition, the mean ± s.d. are represented (Arterioles: 1.57 ± 1.05 Pa – Venules: 0.31 ± 0.35 Pa). (B) Schematics of the microfluidic setup under flow conditions, controlled by a syringe pump. (C) Representative images of nucleus alignment (top) and the circular plot of orientation (bottom). (D-E) Graph of nucleus interquartile range (orientation), and nucleus elongation. Each dot corresponds to the mean value of one vessel. For each condition, the mean ± s.d. are represented (No flow conditions: 53.0 ± 30.2° and 1.63 ± 0.109 a.u. – 24h of flow: 12.9 ± 4.59° and 2.01 ± 0.232 a.u.). All statistics have been computed with Wilcoxon tests.

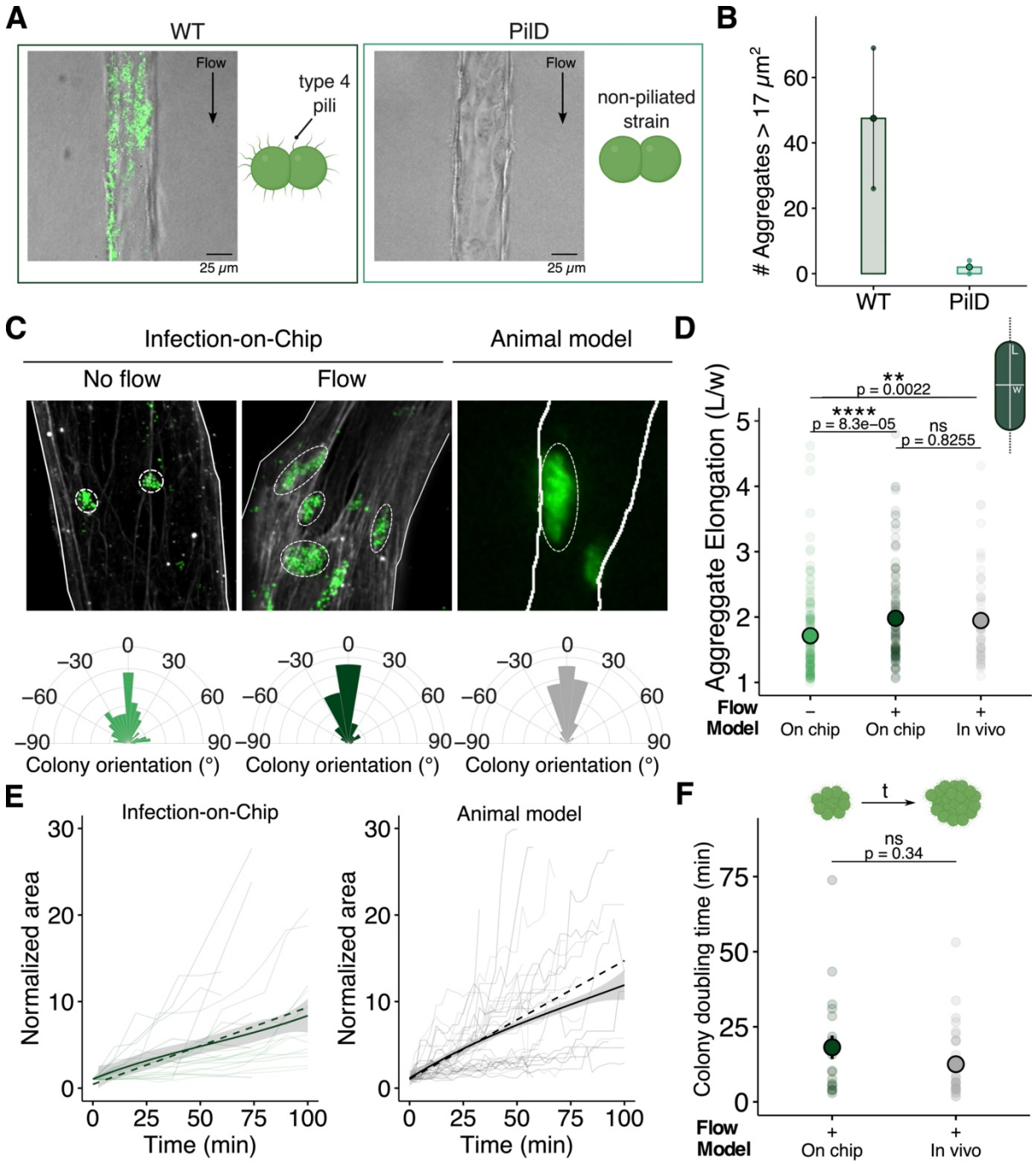

Fig. 5: Liquid flow impacts microbial colony morphologies

(A) Bright field and fluorescence confocal images of Infection-on-Chips after 3h of infection with WT (left) and *pilD* (right) *N. meningitidis* strains. (B) Graph representing the number of aggregates after 3h of infection with WT and *pilD N. meningitidis* strains. (C) Confocal images of WT microcolonies

formed on the vascular wall after 3h of infection in the case of steady state (Infection-on-Chip), under flow conditions (Infection-on-Chip), and in animal model (top). Circular plots representing the distribution of colony orientation (bottom). (D) Graph representing elongation of bacterial colonies after 3h of infection. Each dot corresponds to a bacterial colony. For each condition, the mean ± s.d. are represented (Infection-on-Chip, $Flow^{-}$: 1.75 ± 0.77 – Infection-on-Chip, $Flow^{+}$: 2.11 ± 1.02 – Animal model: 2.07 ± 0.971). (E) Normalized surface area of colonies over time, in Infection-on-Chip (left) and in human skin-grafted mice vessels (right). Solid thin curves, solid thick curves, and dashed thick curves represent individual colony growth, mean, and linear fit ($y = ax + 1$), respectively. (F) Colony expansion time extracted from the previous curves (1/a). Each dot corresponds to a bacterial colony. For each condition, the mean ± s.d. are represented (Infection-on-Chip: 26.2 ± 40.4 min – Animal model: 15.2 ± 18.8 min). All statistics have been computed with Wilcoxon tests.

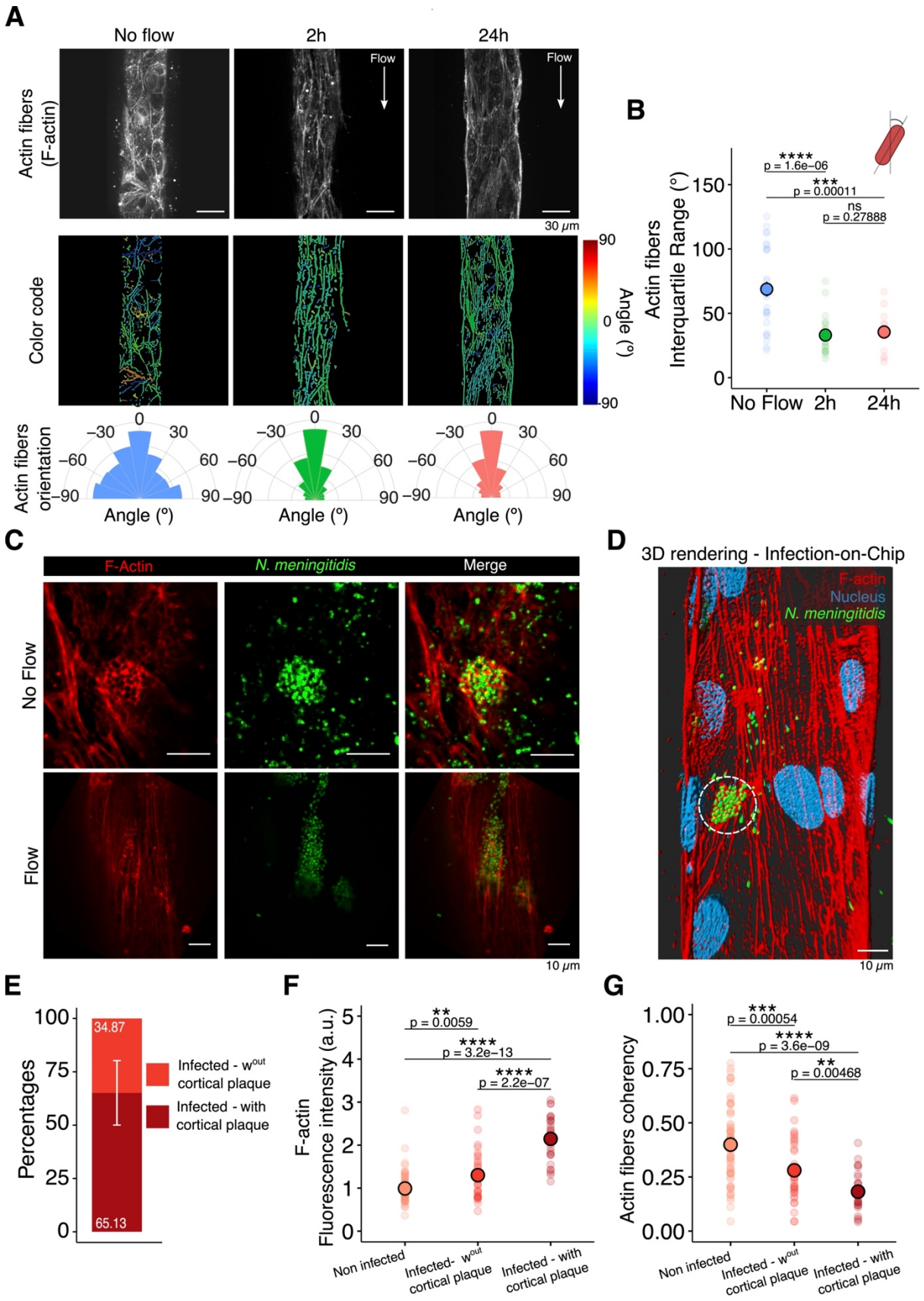
A
No flow
2h
24h
Flow
Flow
Actin fibers (F-actin)
30 µm
Color code
90
0
-90
Angle (°)
Actin fibers orientation
Angle (°)
B
Actin fibers Interquartile Range (°)
****
p = 1.6e−06
***
p = 0.00011
ns
p = 0.27888
No Flow
2h
24h
C
F-Actin
N. meningitidis
Merge
No Flow
Flow
10 µm
D
3D rendering - Infection-on-Chip
F-actin
Nucleus
N. meningitidis
10 µm
E
Percentages
34.87
65.13
Infected - w^out cortical plaque
Infected - with cortical plaque
F
F-actin Fluorescence intensity (a.u.)
**
p = 0.0059
****
p = 3.2e−13
****
p = 2.2e−07
Non infected
Infected- w^out cortical plaque
Infected - with cortical plaque
G
Actin fibers coherency
***
p = 0.00054
****
p = 3.6e−09
**
p = 0.00468
Non infected
Infected - w^out cortical plaque
Infected - with cortical plaque

410

411 **Fig. 6: Flow-induced aligned actin stress fibers are reorganized below bacterial microcolonies**

412 (A) Confocal images of the F-actin network without flow, after 2h and 24h of flow (top). Corresponding
413 segmented images. Blue and red colors represent the perpendicular fibers compared to flow direction,
414 and green/yellow colors represent the parallel fibers to flow direction (middle). Circular plots of total
415 numbers of actin fibers (bottom). (B) Interquartile range of F-actin fiber orientation. (C) Confocal
416 images of honeycomb-shaped cortical plaque formed by *N. meningitidis* colonies without flow (top)
417 and under flow conditions (bottom). (D) 3D rendering of a vessel infected with *N. meningitidis* after 3h
418 of infection under flow conditions. (E) Percentages of colonies forming cortical plaques. (F) F-actin
419 fluorescence intensity. Each dot represents a colony. For each condition, the mean ± s.d. are represented
420 (Not infected regions: 0.99 ± 0.33 a.u. – Infection, without cortical plaque: 1.30 ± 0.57 a.u. – Infection,
421 with cortical plaque: 2.15 ± 0.54 a.u.). (G) Coherency of actin fibers on non-infected regions and on
422 infection sites. Each dot represents a colony. For each condition, the mean ± s.d. are represented (Not
423 infected regions: 0.40 ± 0.17 a.u. – Infection, without cortical plaque: 0.28 ± 0.15 a.u. – Infection, with
424 cortical plaque: 0.18 ± 0.09 a.u.). All statistics have been computed with Wilcoxon tests.

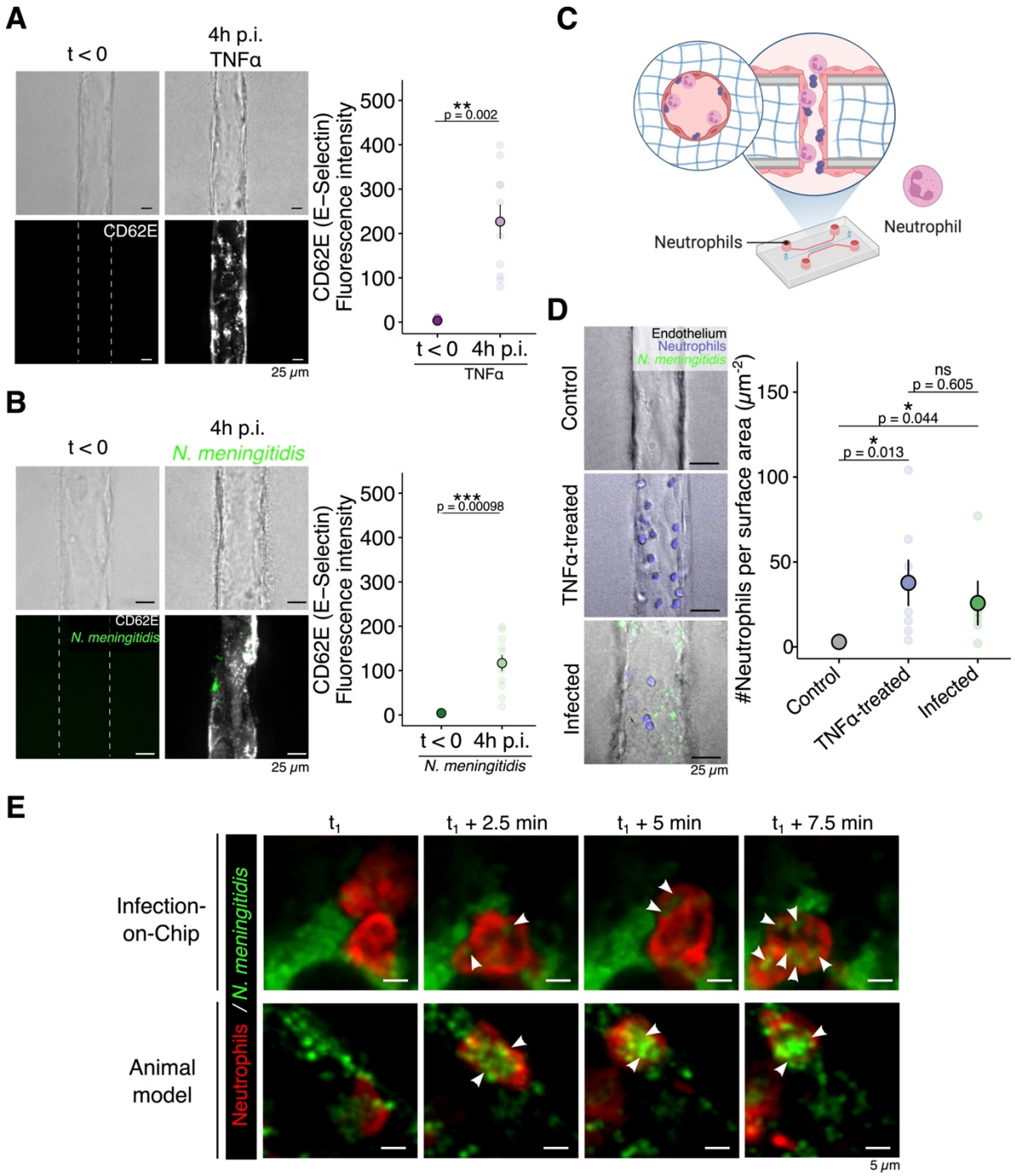

425

426 **Fig. 7: Infection-on-chip recapitulates the human neutrophil response to *N. meningitidis***

427 **infection**

428 (A) Bright field and fluorescence confocal images of a Vessel-on-Chip before and after 4h of TNFα

429 treatment (left). Graph of the global expression of E-selectin (right). Each dot represents a vessel. For

each condition, the mean ± s.d. are represented (TNFα: Before treatment: 1.85 ± 3.85 – 4h post treatment: 224.0 ± 93.7). (B) Bright field and fluorescence confocal images of a Vessel-on-Chip before and after 4h of *N. meningitidis* infection (left). Graph of the global expression of E-selectin (right). Each dot represents a vessel. For each condition, the mean ± s.d. are represented (*N. meningitidis*: Before infection: 1.42 ± 1.02 – 4h p.i.: 105.0 ± 54.4). (B) Schematic representation of the setup. Purified neutrophils were introduced in the microfluidic chip under flow conditions (0.7-1 µl/min). (D) Bright field and fluorescence confocal images of neutrophils adhering on a non-treated (control), TNFα-treated and *N. meningitidis* infected VoC (left). Graph representing the total number of neutrophils adhering to endothelium for each condition (right). Each dot represents a vessel. For each condition, the mean ± s.d. are represented (Control: 0.59 ± 1.32 μm^2 – TNFα: 33.0 ± 36.1 μm^2 – *N. meningitidis*: 21.5 ± 28.4 μm^2). (E) Phagocytosis events of neutrophils in infected VoC (top) and in infected human vessel in the grafted mice (bottom).

442

443

444 **Materials and Methods**

445 ***Bacteria strains and culture***. Infections were performed using *N. meningitidis* strains derived from the
446 8013 serogroup C strain (http://www.genoscope.cns.fr/agc/nemesys) [63]. Mutations in *pilD* gene have
447 been previously described [63]. Wild-type and *pilD* bacterial strains were genetically modified to
448 constitutively express either the green fluorescent protein (GFP) [40, 43], the mScarlet fluorescent
449 protein (mScar) or the near-infrared fluorescent protein (iRFP) under the control of the *pilE* gene
450 promoter [11, 45].

451 Strains were streaked from -80 °C freezer stock onto GCB agar plates and grown overnight (5% CO_2,
452 37 °C). For all experiments, bacteria were transferred to liquid cultures in pre-warmed RPMI-1640
453 medium (Gibco) supplemented with 10% FBS at adjusted OD_{600nm} = 0.05 and incubated with gentle
454 agitation for 2 h at 37 °C in the presence of 5% CO_2.

455

456 ***Microfabrication***. The microfluidic chip was designed on Clewin™ 5.4 (WieWeb software). The
457 corresponding photolithography mask was ordered from Micro Lithography Services LTD
458 (Chelmsford, UK). The chip molds were created by means of photolithography on an MJB4 mask
459 aligner (Süss MicroTec, Germany). Briefly, SUEX-K200 resin (DJ Microlaminates Inc., US) was
460 laminated onto a 4-inch silicon wafer. Lamination temperature, baking, UV exposure dose, and
461 development steps were performed according to the manufacturer recommendations to produce molds
462 with a 200 mm height. Obtained heights were verified with a contact profiler (DektakXT, Bruker). After
463 overnight silanization, (Trichloro(1H,1H,2H,2H-perfluorooctyl)silane, Sigma-Aldrich) replication of
464 the devices was performed with poly-dimethyl-siloxane (PDMS, Silgard 184; Dow Chemical). After
465 polymerization, PDMS slabs were cut and punched to form inlets and outlets (1 and/or 4 mm^2 for lateral
466 channels, 1 mm^2 for central channel). Bonding onto glass-bottom ibidi dishes (Ref. 81158) was

467 performed with a Cute plasma cleaner (Femto science, Kr). Critically, assembled microfluidic chips
468 were heated at 80ºC for 48h to insure both robust bonding and nominal PDMS hydrophobicity to allow
469 consecutive hydrogel loading.

470 Chips were cooled down at 4ºC for at least 8h to avoid quick polymerization while introducing the
471 hydrogel in the chip. The collagen I solution was introduced in the center channel (see **Fig. 1**). FujiFilm
472 collagen I (LabChem Wako, Collagen-Gel Culturing Kit) has been used to obtain the 2.4 mg/ml
473 solution, while the high concentration collagen I (Corning, #354249) has been used to obtain the 6
474 mg/ml, 4 mg/ml, and 3.5 mg/ml solutions according to the manufacturer's protocol. After collagen
475 polymerization at 37ºC for 20 min, PBS (Gibco) was added to the chips via the large lateral channels to
476 avoid hydrogel drying. The inlet and outlet of the hydrogel channel were blocked with a droplet of
477 liquid PDMS. Finally, chips were incubated at 37ºC for several hours to complete the hydrogel
478 polymerization.

479 The collagen I matrix was carved using a pulsed UV laser (MOPA-355, 500mW) focused through a
480 20x objective with NA=0.7 (UCPLFLN20X). The chip was then displaced with the microscope stage
481 (SCANPLUS-IM, Marzhauser Wetzlar) at 1 mm/s to control ablation region. Laser intensity was
482 checked before each experiment to ensure a proper laser alignment using a light sensor (Thorlabs, Power
483 sensor head S170C and Power Meter for Laser, PM100A). Laser power under the sample was adjusted
484 at 10 mW. The geometries of vessels have been designed with FUSION 360 (AutoCAD) or extracted
485 from intravital microscopy images, exported on a .png binary image and called in the python code.

486

487 ***Cell culture***. Primary human umbilical endothelial cells (HUVECs) were purchased from Lonza
488 (pooled donors, # C2519A) and cultured in EGM-2 complete medium (Lonza, # CC-3162) in untreated
489 75 cm^2 flasks – 37ºC, 5% CO_2. Cells were used between passages 2 and 6. Before passage or chip
490 endothelialisation, HUVEC were detached with 3 mL of Trypsin/EDTA (Gibco) for 4 min at RT. The
491 cell/Trypsin/EDTA suspension was diluted with 4 mL of EGM-2 medium and centrifugated for 5 min

492 at 1200 RPM (i.e. 300 G). After supernatant removal, the cell pallet is diluted at 1/3 for passage and
493 concentrated at 14 x10^6 cells/mL for chip endothelialisation.

494 Before endothelialization, chips were washed twice with warm EGM-2 medium. The media was
495 partially removed (to avoid bubbles in the system) and 5 µL of the 14M cells/mL suspension were
496 introduced in the chip via a lateral channel (see **Fig. 1**). Chips were incubated (filled channel on the top)
497 for 30 min. The same operation was repeated for the other channel. After 1h of total incubation, chips
498 were gently washed with EGM-2 medium to remove non-adherent cells and incubated for 12h.

499 The flow was added to the setup 12h after cell seeding/during infection/upon neutrophils experiments:
500 syringes (SGE, 2.5 mL, glass) were connected to the chips (needle: SGE™ Gastight Syringes, tubings:
501 tygon – Saint-Gobain, ID 0.02 mm and OD 0.06 mm / PTFE - Merck) and controlled via a syringe-
502 pump (Cetoni). Microfluidic chips were kept at 37ºC - 5% CO_2 for at least 24h.

503 For TNFα treatment, a solution of 50 ng/mL (Sigma, #H8916) has been introduced in chips for 4h
504 (37ºC, 5% CO_2) to induce inflammation on the endothelium.

505

506 ***Mice***. SCID/Beige (CB17.Cg-PrkdcscidLystbg-J/Crl) mice were used in all the experiments (Central
507 Animal Facility, Institut Pasteur, Paris, France). Mice were housed under the specific pathogen-free
508 condition at Institut Pasteur. Mice were kept under standard conditions (light 07.00–19.00 h;
509 temperature 22 ± 1°C; humidity 50 ± 10%) and received sterilized rodent feed and water ad libitum. All
510 experiments were performed in agreement with guidelines established by the French and European
511 regulations for the care and use of laboratory animals and approved by the Institut Pasteur Committee
512 on Animal Welfare (CETEA) under the protocol code CETEA 2018-0022. For all experiments, male
513 and female mice between 6 and 13 weeks of age were used. Littermates were randomly assigned to
514 experimental groups.

515

516 ***Xenograft model of infection***. Five to eight weeks old mice, both males and females, were grafted with
517 human skin as previously described [11]. Briefly, a graft bed of ~1cm^2 was prepared on the flank of
518 anesthetized mice (intraperitoneal injection of ketamine and xylazine at 100 mg/kg and 8.5 mg/kg,
519 respectively) by removing the mouse epithelium and the upper dermis layer. A human skin graft of
520 about 200-µm thick comprising the human epidermis and the papillary dermis was immediately placed
521 over the graft bed. Grafts were fixed in place with surgical glue (Vetbond, 3 M, USA) and dressings
522 were applied for 1 week. Grafted mice were used for experimentation 4-10 weeks post-surgery when
523 the human dermal microvasculature is anastomosed to the mouse circulation without evidence of local
524 inflammation, as previously described [11].

525 Normal human skin was obtained from adult patients (20–60 years old), both males and females,
526 undergoing plastic surgery in the service de Chirurgie Reconstructrice et Plastique of Groupe
527 Hospitalier Saint Joseph (Paris, France). In accordance with the French legislation, patients were
528 informed and did not refuse to participate in the study. All procedures were approved by the local ethical
529 committee Comité d'Evaluation Ethique de l'INSERM IRB 00003888 FWA 00005881, Paris, France
530 Opinion: 11048.

531

532 ***Immunofluorescence staining***. Collagen gels have been stained with a Maleimide Alexa Fluor™ 488
533 (ThermoFisher, #A10254) solution: 10 µL of Maleimide (100 µg/ml) has been diluted within 700 µL
534 of a 0.2 M sodium bicarbonate buffer solution. Chips were incubated with this solution for 1h at RT in
535 dark, and finally gently washed with PBS before imaging.

536 For E-Selectin experiments, before and after TNFα treatment or infection, a solution of 10^{-3} mg/ml PE-
537 conjugated anti-human CD62E (clone P2H3, Thermofisher Scientific, #12-0627-42) has been
538 introduced in the chips to stain the endothelium for 10 min. After gentle washing steps with EGM-2
539 medium, CD62E expression was acquired (Nikon, Spinning disk, Obj. 20X, dry, NA=0.75).

540 Chips were fixed with PFA 4%v/v for 15 min, permeabilized with Triton X-100 1%v/v for 30 min,
541 blocked with PBS-gelatin 1%v/v for 15 min, and mounted with fluoromount-G solution (Fluoromount-
542 G, SouthernBiotech, #0100-01). Chips were incubated with Phalloidin at 0.66 µM (Alexa Fluor 488,
543 Thermofisher, #A12379), anti-human PECAM antibody at 2.5 x10^{-3} mg/ml (DyLight 550 NHS-Ester
544 #62263), anti-human collagen IV antibody at 10^{-2} mg/ml (Alexa Fluor 642, Clone 1042, eBioscience
545 #51-9871-82) for 10h at 4ºC, and Hoechst 10^{-2} mg/ml (33362 trihydrochloride trihydrate, invitrogen
546 #H3570) has been added right before adding the mounting solution.

547 Human and mice skin samples were fixed with PFA 4%/PBS overnight, washed 3 times in PBS (30
548 min of incubation time for each) and blocked with buffer (0,3% triton + 1% BSA + 1% NGS in PBS)
549 overnight at 4°C. Samples were stained 3 days at 4ºC with phalloidin (0.66 µM, Alexa Fluor 488,
550 Thermofisher, #A12379) and DAPI (0.3 mg/ml, ThermoFisher, #62247) overnight at 4ºC. A sample
551 clear was made with a Rapid clear 1,47 medium for 2 days at room temperature and a mounting solution
552 was introduced between slide and cover-slide in rapid clear medium.

553

554 ***Microscopy imaging.*** Dynamics of bacteria growth during 3h and neutrophil adhesion during 1h were
555 followed with a Nikon Spinning Disk, 20X NA=0.75 objective lens, under 5% CO_2, at 37ºC.
556 Fluorescence signals were detected using a sCMOS 2048 × 2048-pixel camera (Orca Flash v2 +,
557 Hamamatsu). Metamorph acquisition software was used to drive the confocal microscope.

558 Fixed samples have been imaged either with a Leica Spinning disk DM6 FS upright microscope, HCX
559 PL Fluotar 5X - NA=0.15, HC Fluotar 25X - NA=0.95 and HC PL APO 40X - NA=1.10 objective lens;
560 and/or a Andor confocal BC43 upright microscope, 40X objective lens.

561 Intravital imaging of the human xenograft was adapted from [64]. Briefly, 30-min prior to surgery, mice
562 were injected subcutaneously with buprenorphine (0.05 mg/kg) and anesthetized by spontaneous
563 inhalation of isoflurane in 100% oxygen (induction: 4%; maintenance: 1.5% at 0.3 L/min). A middle
564 dorsal incision was made from the neck to the lower back and the skin supporting the human xenograft

565 was flipped and secured onto an aluminum custom-made heated deck (36°C). The human
566 microvasculature within the graft was exposed by carefully removing the excess of connective tissue.
567 The skin flap was covered with a coverslip and maintained thanks to a 3D-printed custom-made holder
568 to avoid any pressure on the xenograft vasculature, sealed with vacuum grease, and continuously
569 moistened with warmed 1× PBS (36°C). Mice hydration was maintained by intraperitoneal injection of
570 200 µl 0.9% saline solution every hour. During the experiment, the mouse's body temperature was
571 maintained at 37°C using a heating pad. The tail vein was cannulated allowing the injection of
572 fluorescent dyes and/or bacteria. In all experiments, human vessels were labelled using fluorescently
573 conjugated UEA-1 lectin (100 µg, Dylight 650 or Dylight755, Vector Laboratories) and five to ten
574 fields of view of interest containing human vessels were selected per animal for observations.

575 During intravital imaging of the animal model, mice were anesthetized by spontaneous inhalation of
576 isoflurane in 100% oxygen (induction: 4%; maintenance: 1.5% at 0.3 L/min) and placed in ventral
577 decubitus on a heating pad (37°C) to maintain body temperature. The dorsal face of the ear pinnae was
578 epilated using depilatory cream without causing irritation. The ear was carefully flattened out on an
579 aluminum custom-made heated deck (36°C) and held in place with a coverslip. The tail vein was
580 cannulated allowing the injection of fluorescent dyes.

581 Intravital imaging of the mouse ear and human xenograft skin was performed using a Leica DM6 FS
582 upright microscope equipped with a motorized stage. The microscope is fitted with HCX PL Fluotar
583 5X - NA=0.15, HC Fluotar 25X - NA=0.95 and HC PL APO 40X - NA=1.10 objective lens (Leica),
584 mounted on an optical table to minimize vibration and totally enclosed in a biosafety cabinet (Noroit).
585 The microscope is coupled to a Yokogawa CSU-W1 confocal head modified with Borealis technology
586 (Andor). Four laser excitation wavelengths (488, 561, 642, and 730 nm) were used in fast succession
587 and visualized with the appropriate long-pass filters. Fluorescence signals were detected using a
588 sCMOS 2048 × 2048-pixel camera (Orca Flash v2 +, Hamamatsu). Metamorph acquisition software
589 was used to drive the confocal microscope.

590 The images were exported from the Metamorph acquisition software (Molecular Devices) as .tiff files
591 and edited using Fiji. Movies were exported as .avi files and edited on Final Cut Pro (Apple). Image
592 analysis has been achieved with ImageJ2 (version 2.9.0/1.53t).

593

594 ***Permeability assays***. In VoC, 10 µL of a 0.1 mg/mL dextran solution (FITC, Sigma) have been
595 introduced in chips during 45 min.

596 *In vivo,* mice were intravenously injected with 20 µg of anti-mouse CD31 antibodies coupled with Alexa
597 Fluor 647 (clone 390, Biolegend) to label blood vessels and ear was allowed to stabilize for 30 min.
598 Prior to imaging, 5 mg of fluorescein isothiocyanate (FITC) conjugated 150 kDa dextran (Sigma-
599 Aldrich, St Louis, MO) dissolved in 200 ml of phosphate buffered saline (PBS) were injected
600 intravenously. Stacks of 10 images, spaced 4 mm apart, were acquired every minute.

601 For both models, The permeability has been quantified over the first 15 min, following the equation:

602 $$P = \frac{R}{2}\frac{1}{\Delta I_0^{channel}}\left(\frac{dI^{collagen}}{dt}\right)$$

603 Where R is the channel radius, $\Delta I_0^{channel}$ the first step in increase of fluorescence in the channel, and
604 $\frac{dI^{collagen}}{dt}$ the rate of increase in fluorescence in the collagen matrix.

605

606 ***Imaging Particle Image Velocimetry (PIV)***. *In vivo*, basal microvascular blood flow in human vessels
607 (arterioles and venules) was measured by high-speed acquisitions on a single plane (50 frames per
608 second, 300 frames) of intravenously perfused (15 µl/min) 1 µm large fluorescent microspheres
609 (Yellow/Green Fluoresbrite carboxylate, Polysciences, 107 microspheres/ml 1x PBS). Speed was
610 determined from the centerline microsphere. Blood flow of each vessel was then computed from vessel
611 surface section and mean velocity following: $Q_{blood} = V_{bead}^{mean}.S_{vessel}$

612

613 ***Neutrophil adhesion and phagocytosis.*** *In vitro*, human neutrophils have been purified from donor
614 blood. Human peripheral blood samples were collected from healthy volunteers through the ICAReB-
615 Clin (Clinical Investigation platform) of the Institute Pasteur [65]. All participants received an oral and
616 written information about the research and gave written informed consent in the frame of the healthy
617 volunteers CoSImmGEn cohort (Clinical trials NCT 03925272), after approval of the CPP Ile-de-
618 France I Ethics Committee (2011, jan 18th) [65]. Neutrophils have been stained for nucleus (Hoechst,
619 10^{-3} mg/ml, 33362 trihydrochloride trihydrate, invitrogen #H3570)) and actin (SPY555-actin, 1/1000,
620 Spirochrome #CY-SC202). After 10 min of a TNFα-induced activation (10 ng/mL), 10 µL of a 6 M
621 cells/mL suspension has been introduced in the chips. After, the flow has been then added to the system
622 at 0.7-1 µl/min. Human neutrophils adhesion and phagocytosis have been acquired within 1h at 37ºC
623 and 5% CO_2.

624 In the animal model, after 2h of liquid culture, bacteria were washed twice in PBS and resuspended to
625 10^8 CFU ml^{-1} in PBS. Prior to infection, mice were injected intraperitoneally with 8 mg of human
626 transferrin (Sigma Aldrich) to promote bacterial growth *in vivo*, as previously described [63] and
627 neutrophils were labelled by were labeled with 2.5 µg Dylight550-conjugated anti-mouse Ly-6G (LEAF
628 purified anti-mouse Ly-6G, clone 1A8, Biolegend, #127620 + DyLight550 Antibody Labelling Kit,
629 ThermoFisher Scientific, #84530). Mice were infected by intravenous injection of 100 µl of the bacterial
630 inoculum (10^7 CFU total) and time-lapse z-stack series (2-2.5 µm z-step, 50-80 µm range) were
631 captured every 20 min for 3 hours to image bacterial growth and every 30 sec for 20 min to image
632 phagocytosis of bacteria by neutrophils.

633

634 ***Rheology asssays***. Collagen gels visco-elastic properties were measured using an Ultra+ rheometer
635 (Kinexus). 200 µL of collagen gel were placed at the center of the rheometer plate kept at 4ºC plate.
636 The 20 mm-diameter testing geometry was lowered to a gap of 200 µm. Excess of hydrogel was

removed. Temperature was ramped up to 37ºC (within 60 sec) to initiate the hydrogel formation. Gelation dynamics and gel properties were extracted from continuous geometry rotation at 1 Hz frequency and a 1% strain. Rheological values i.e. elastic modulus G' stabilized after 200 sec. Final values were determined by averaging values between 500 and 700 sec.

A*ctin fiber alignment / nucleus alignment and elongation*. The z projection (Maximum Intensity) of the top and bottom parts of vessels have been realized for actin fibers and nucleus segmentation and analysis. Only the images taken with Leica Spinning disk microscope, 40X, NA=1.10 (see below for more details) were used for analyses. The fibers and the nuclei located at the vessel edges have been excluded from the analysis. The angle and the ratio major/minor axis have been measured for all vessels (circular plots) and averaged by vessel (dotted graph).

For *in vivo* images, the segmentation of nuclei has been achieved by hand for several z slices for each vessel. The alignment (angle) and elongation (ratio major/minor) have been measured for all vessels (circular plots) and averaged by vessel (dotted graph).

In vitro *actin recruitment and coherency*. The z projection (Maximum Intensity) of the top and bottom parts of vessel (taken with the 40X, NA=1.10 - see below for more details) have been used to quantify actin recruitment and fibers coherency. Region of Interest (ROIs) of similar sizes were located on infected and non-infected areas of the endothelium.

For each ROI, the mean fluorescence intensity has been subtracted by the background intensity (collagen matrix) and normalized by the mean of non-infected areas intensity:

$$I_{actin\ recruitment} = \frac{I_{ROI}^{infected} - I_{background}}{mean(I_{ROI}^{non-infected})}$$

659 The coherency has been assessed with the OrientationJ Measure plugin (BIG, EPFL).

660

661 ***Statistics***. Post-processing and statistics analyses have been realized with R (R Studio version
662 2022.12.0+353, R version 4.2.2 (2022-10-31)). No statistical method was used to predetermine sample
663 size. Statistical tests were based on the Wilcoxon tests – with p-values > 0.05: n.s., 0.05 < p-values <
664 0.01: *, 0.01 < p-values < 0.005: **, 0.005 < p-values < 0.001: ***, p-values < 0.001: ****. Scatter dot
665 plots show the mean ± sd. Statistical details of experiments such as sample size, replicate number,
666 statistical significance, are explicitly added in the figure legends, and source data files.

667

668 **Acknowledgements**

669 We thank P. Vargas, A. Desys and M. Bernard (Leukomotion, Institut Necker Enfants Malades) for
670 their help in the purification of human neutrophils and C. Travaillé (Photonic Bioimaging, Institut Pas-
671 teur) for complementary microfluidic chip imaging. We are grateful to the healthy volunteers of blood
672 donation, for their participation in the study. We thank ICAReB-Clin of the Medical Direction and
673 ICAReB-biobank of the CRBIP (BioResource Center) of the Institut Pasteur (Paris) for providing blood
674 samples from healthy volunteers. To H. Laude, L. Arowas, B. L. Perlaza, A. Z. M. Delhaye and C.
675 Noury for managing the participants' visits. To E. Roux, R. Artus, L. Sangari, D. Cheval, S. Vacant,
676 for preparing the blood samples from donors.

677

678 **Fundings**

679 The work was supported by the IBEID Labex fellowship [grant number 10-LBX-62] and NRJ founda-
680 tion for L.P. post-doctoral fundings; ANR MeningoChip [grant number ANR 18 CE15 0006 01] and
681 DIM Elicit. All authors declare that they have no conflicts of interest.

682 **References**

683 [1] Murray, J. L. *et al.* Global burden of bacterial antimicrobial resistance in 2019: a systematic analysis.
684 *The Lancet* **399**, 10325, 629-655 (2022)

685 [2] Minasyan, H. *et al.* Sepsis: mechanisms of bacterial injury to the patient. *Scand J Trauma Resusc*
686 *Emerg Med* **27**, 19 (2019)

687 [3] Brandzaeg, P. and Van Deuren, M. Classification and Pathogenesis of Meningococcal Infections,
688 Method in Molecular Biology, 21-35 (2011)

689 [4] Lécuyer, H. *et al.* Pathogenesis of meningococcal purpura fulminans. *Pathogens and Disease* **5**, 3
690 (2017)

691 [5] Melican, K. and Dumenil, G. Vascular colonization by Neisseria meningitidis. *Current Opinion in*
692 *Microbiology* **15**, 1, 50-56 (2012)

693 [6] Saul N Faust, S. N., Heyderman, R. S., Levin, M. Disseminated intravascular coagulation and
694 purpura fulminans secondary to infection, *Best Practice & Research Clinical Haematology* **13**, 2, 179–
695 197 (2000)

696 [7] Guarner, J. *et al.* Pathogenesis and Diagnosis of Human Meningococcal Disease Using
697 Immunohistochemical and PCR Assays. *American Journal of Clinical Pathology* **122**, 5, 754–764
698 (2004)

699 [8] Melican K. *et al.* Adhesion of *Neisseria meningitidis* to Dermal Vessels Leads to Local Vascular
700 Damage and *Purpura* in a Humanized Mouse Model. *PLOS Pathogens* **9**, 1, (2013)

701 [9] Maïssa, N. *et al.* Strength of *Neisseria meningitidis* binding to endothelial cells requires highly-
702 ordered CD147/β_2-adrenoceptor clusters assembled by alpha-actinin-4. *Nat Commun* **8**, 15764 (2017)

[10] Schönherr-Hellec, S. *et al.* Implantation of engineered human microvasculature to study human infectious diseases in mouse models. *iScience* **26**, 106286 (2023)

[11] Manriquez, V. *et al.* Colonization of dermal arterioles by *Neisseria meningitidis* provides a safe haven from neutrophils. *Nat Commun* **12**, 4547 (2021)

[12] Denis, K. *et al.* Targeting Type IV pili as an antivirulence strategy against invasive meningococcal disease. *Nat Microbiol* **4**, 972–984 (2019)

[13] Doulet, N. *et al. Neisseria meningitidis* infection of human endothelial cells interferes with leukocyte transmigration by preventing the formation of endothelial docking structures. *J Cell Biol* **173,** 4, 627–637 (2006)

[14] Bonazzi, D. *et al.* Intermittent Pili-Mediated Forces Fluidize *Neisseria meningitidis* Aggregates Promoting Vascular Colonization. *Cell* **174**, 1, 143–155 (2018)

[15] Eugène, E. *et al.* Microvilli-like structures are associated with the internalization of virulent capsulated *Neisseria meningitidis* into vascular endothelial cells. *J Cell Sci* **115,** 6, 1231–1241 (2002)

[16] Merz, A. J., So, M. Attachment of piliated, Opa- and Opc- gonococci and meningococci to epithelial cells elicits cortical actin rearrangements and clustering of tyrosine-phosphorylated proteins. *Infection and Immunity* **65,** 10, 4341 - 4349 (1997)

[17] Wang, B. *et al.* A comparative study unraveling the effects of TNF-α stimulation on endothelial cells between 2D and 3D culture. *Biomed. Mater* **15,** (2020)

[18] Ko, J. *et al.* Human Ocular Angiogenesis-Inspired Vascular Models on an Injection-Molded Microfluidic Chip. *Adv. Healthcare Mater.* **8,** 1900328 (2019)

[19] Haase, K. *et al.* Endothelial Regulation of Drug Transport in a 3D Vascularized Tumor Model. *Adv. Funct. Mater* **30,** 2002444 (2020)

[20] O'Connor, C. *et al.* Engineering the multiscale complexity of vascular networks. *Nat Rev Mater* **7**, 702–716 (2022)

[21] Dessalles, C. A. *et al.* Luminal flow actuation generates coupled shear and strain in a microvessel-on-chip *Biofabrication* **14,** 015003 (2022)

[22] Haase, K. and Kamm, R. D. Advances in on-chip vascularization, *Regenerative Medicine* **12**, 3, 285-302 (2017)

[23] Herland, A. *et al.* Distinct Contributions of Astrocytes and Pericytes to Neuroinflammation Identified in a 3D Human Blood-Brain Barrier on a Chip. *Plos one* **11**, 3, e0150360 (2016)

[24] Brandenberg, N. and Lutolf, M.P. In Situ Patterning of Microfluidic Networks in 3D Cell-Laden Hydrogels. *Adv. Mater.*, 28: 7450-7456 (2016)

[25] Enrico, A. 3D Microvascularized Tissue Models by Laser-Based Cavitation Molding of Collagen. *Adv. Mater.* **34**, 2109823 (2022)

[26] Sarig-Nadir, O. *et al.* Laser Photoablation of Guidance Microchannels into Hydrogels Directs Cell Growth in Three Dimensions. *Biophysical Journal* **96**, 11, 4743-4752 (2009)

[27] Haase, K. *et al.* Physiologic flow-conditioning limits vascular dysfunction in engineered human capillaries. *Biomaterials* **280**, 121248 (2022)

[28] Davis, G. E. and Senger, D. R. Endothelial Extracellular Matrix: Biosynthesis, Remodeling, and Functions During Vascular Morphogenesis and Neovessel Stabilization. *Circulation Research* **95**, 11 (2005)

[29] Kular, J. K. *et al.* The extracellular matrix: Structure, composition, age-related differences, tools for analysis and applications for tissue engineering. *Journal of Tissue Engineering* **5** (2014)

[30] Leclech, C., Natale, C., and Barakat, A.I. The basement membrane as a structured surface – role in vascular health and disease. *Journal of Cell Science* **133** (2020)

[31] Zhou, H. L. *et al.* Role of blood flow in endothelial functionality: a review. *Cell Dev. Biol*. **11** (2023)

[32] Mairey. E. *et al.* Cerebral microcirculation shear stress levels determine *Neisseria meningitidis* attachment sites along the blood–brain barrier. *J Exp Med* **203,** 8, 1939–1950 (2006)

[33] Pries, A. R., Secomb, T. W. and Gaehtgens, P. Design Principles of Vascular Beds. *Circulation Research* **77**, 5, 1017–1023 (1995)

[34] Peng, Z., *et al.* Endothelial Response to Pathophysiological Stress. *Arteriosclerosis, Thrombosis, and Vascular Biology* **39,** 233–243 (2019)

[35] Osinnski, J. N., *et al.* Determination of wall shear stress in the aorta with the use of MR phase velocity mapping. *J. Magn. Reson. Imaging* **5,** 640–647 (1995)

[36] Davies, P. F. Flow-mediated endothelial mechanotransduction. *Physiological Reviews* **75,** 3, 519-560 (1995)

[37] Tkachenko, E. *et al.* The nucleus of endothelial cell as a sensor of blood flow direction. *Biol Open* **2,** 10, 1007–1012 (2013)

[38] Ershov, D. *et al.* TrackMate 7: integrating state-of-the-art segmentation algorithms into tracking pipelines. *Nat Methods* **19**, 829–832 (2022)

[39] Rossy T., *et al. Pseudomonas aeruginosa* type IV pili actively induce mucus contraction to form biofilms in tissue-engineered human airways. *PLOS Biology* **21,** 8, e3002209 (2023)

[40] Dos Santos Souza I., *et al.* Meningococcal disease: A paradigm of type-IV pilus dependent pathogenesis. *Cell Microbiol* **22,** 4, e13185 (2020)

768 [41] Charles-Orszag, A. *et al.* Adhesion to nanofibers drives cell membrane remodeling through one-
769 dimensional wetting. *Nat Commun* **9**, 4450 (2018)

770 [42] Bernard, S. *et al.* Pathogenic *Neisseria meningitidis* utilizes CD147 for vascular colonization. *Nat*
771 *Med* **20**, 725–731 (2014)

772 [43] Malek, A. M., and Izumo, S. Mechanism of endothelial cell shape change and cytoskeletal
773 remodeling in response to fluid shear stress. *J Cell Sci* **109**, 4, 713–726 (1996)

774 [44] Davies, P. Hemodynamic shear stress and the endothelium in cardiovascular pathophysiology. *Nat*
775 *Rev Cardiol* **6**, 16–26 (2009)

776 [45] Soyer, M. *et al.* Plasma membrane reshaping by adhering meningococci. *Cell Microbiol* **16**, 878-
777 895 (2014)

778 [46] Ley, K. *et al.* Getting to the site of inflammation: the leukocyte adhesion cascade updated. *Nat Rev*
779 *Immunol* **7**, 678–689 (2007)

780 [47] Kumar, A. *et al.* Actomyosin contractility rotates the cell nucleus. *Sci Rep* **4**, 3781 (2014)

781 [48] Virji, M. *et al.* Pilus-facilitated adherence of *Neisseria meningitidis* to human epithelial and
782 endothelial cells: modulation of adherence phenotype occurs concurrently with changes in primary
783 amino acid sequence and the glycosylation status of pilin. *Molecular Microbiology* **10,** 1013-1028
784 (1993)

785 [49] Barnier J. P. *et al.* Type IV pilus retraction enables sustained bacteremia and plays a key role in
786 the outcome of meningococcal sepsis in a humanized mouse model. *PLOS Pathogens* **17,** 2, e1009299
787 (2021)

788 [50] Craig, L., Forest, K.T. & Maier, B. Type IV pili: dynamics, biophysics and functional
789 consequences. *Nat Rev Microbiol* **17**, 429–440 (2019)

[51] Welker, A. *et al.* Molecular Motors Govern Liquidlike Ordering and Fusion Dynamics of Bacterial Colonies *Phys. Rev. Lett.* **121**, 118102 (2018)

[52] Mikaty G., *et al.* Extracellular Bacterial Pathogen Induces Host Cell Surface Reorganization to Resist Shear Stress. *PLOS Pathogens* **5**, 2, e1000314 (2009)

[53] van den Wijngaard, J. P.H.M. *et al.* 3D Imaging of vascular networks for biophysical modeling of perfusion distribution within the heart, *Journal of Biomechanics* **46**, 2, 229–239 (2013)

[54] Piccinelli, M. *et al.* A Framework for Geometric Analysis of Vascular Structures: Application to Cerebral Aneurysms. *IEEE Transactions on Medical Imaging* **28**, 8, 1141–1155 (2009)

[55] Potente, M. and Mäkinen, T. Vascular heterogeneity and specialization in development and disease. *Nat Rev Mol Cell Biol* **18**, 477–494 (2017)

[56] Li, Y. *et al.*. Diabetic vascular diseases: molecular mechanisms and therapeutic strategies. *Signal Transduct Target Ther* **8,** 1, 152 (2023)

[57] Core, J. P. Anti-thrombotic treatment enhances antibiotic efficiency in a humanized model of meningococcemia, *BioRXiv* (2022)

[58] Middelkamp, H. *et al.* Embedded macrophages induce intravascular coagulation in 3D blood vessel-on-chip. *Biomed Microdevices* **26**, 2 (2024)

[59] Rahman, M. M. *et al.* The Gut Microbiota (Microbiome) in Cardiovascular Disease and Its Therapeutic Regulation. *Front. Cell. Infect. Microbiol* **12,** 903570 (2022)

[60] Obino, D. and Duménil, G. The Many Faces of Bacterium-Endothelium Interactions during Systemic Infections, *Microbiology Spectrum* **7**, 2 (2019)

[61] Urbaniak, C. *et al.* Microbiota of Human Breast Tissue. *Applied and Environmental Microbiology* **80**, 10 (2014)

[62] Nejman, D. *et al.,* The human tumor microbiome is composed of tumor type–specific intracellular bacteria. *Science* **368**, 973-980 (2020)

[63] Rusniok, C. *et al.* NeMeSys: a biological resource for narrowing the gap between sequence and function in the human pathogen *Neisseria meningitidis*. *Genome Biol* **10**, R110 (2009)

[64] Ho, M. *et al.* Visualization of *Plasmodium falciparum*–Endothelium Interactions in Human Microvasculature: Mimicry of Leukocyte Recruitment. *J Exp Med* **192,** 8, 1205–1212 (2000)

[65] Esterre, P. *et al.* The ICAReB Platform: The ICAReB Platform: A Human Biobank for the Institut Pasteur and Beyond. *Open Journal of Bioresources* **7**, 1, 1 (2020) BB-0033-00062, BBMRI A0203/ 4 distributions/ last access: 2023, 07, 18; [Whole Blood]